JOURNAL OF THERMOPHYSICS AND HEAT TRANSFER
Vol. 9, No. 4, October–December 1995

Effect of Line Doppler Shift on Plume Infrared Signatures

C. R. Hewitt Jr.*
Ball Corporation, Fairborn, Ohio 45324
and
W. Z. Black†
Georgia Institute of Technology, Atlanta, Georgia 30332

Plume infrared signatures are calculated using narrow-band models because reasonably accurate results are provided relatively quickly for most cases. In certain cases, however, current narrow-band models ignore phenomena that significantly affect the apparent plume signature. One commonly ignored phenomenon is line Doppler shifting (LDS). LDS effects become important when a relative velocity exists between gas layers. Calculation of apparent plume signatures is such a case. A modified narrow-band model has been developed whereby the effect of LDS is approximated in the calculation of the equivalent width. The modification relies on an algebraic relation that is functionally dependent on the emitting layer optical depth, the absorbing layer optical depth, the line-shape parameters, and the line Doppler shift. Broadband radiance results predicted by the new method are compared with line-by-line (LBL) model and standard narrow-band model calculations. The new model is shown to predict absolute increases in apparent radiance on the order of that predicted using LBL techniques.

Nomenclature

A = coefficient in the shifted equivalent width model, Eqs. (10) and (14)
b_3 = coefficient in formula for absorber optical depth at peak ratio of equivalent widths, Eq. (17)
b_4 = coefficient in formula for absorber optical depth at peak ratio of equivalent widths, Eq. (17)
c = speed of light, m/s
d = coefficients in formula for peak ratio of equivalent widths, Eq. (15)
f = line Doppler shift correction factor, Eqs. (2) and (9)
g = shape function within f, Eqs. (9) and (10)
k = spectral absorption cross section, m^2
N = total layers along line of sight
P = pressure, MPa
Su = optical depth, cm^{-1}
s = physical distance along line of sight, m
T = temperature, K
V = relative velocity component along the line of sight, m/s
W = equivalent width, cm^{-1}
x = dummy variable in Eqs. (15) and (16)
x^* = dummy variable in Eqs. (10–14)
y = linearized dependent variable, Eq. (12)
y^* = modeled dependent variable, Eq. (13)
γ = broadened linewidth, cm^{-1}
$\Delta\nu_D$ = line Doppler shift, cm^{-1}
K = coefficient in Eq. (5)
ν = wave number, cm^{-1}
ξ = ratio of linewidth ratios, Eq. (6)
ρ = number density, m^{-3}

Subscripts
a = absorbing layer
D = Doppler broadened, or line Doppler shifted
e = emitting layer
i = layer counter, or summation counter
L = Lorentz broadened
n = summation counter
peak = point of function maximum
s = including line Doppler shifting
u = not including line Doppler shifting
0 = line center or reference condition

Introduction

PLUME infrared (IR) signatures are frequently used to detect and track aircraft and missiles. As a result, designers of IR detection and tracking systems frequently require predictions of plume radiant intensity to assist in determining system operational parameters. Likewise, airframe and missile designers require knowledge of the total aircraft signature, including the plume, in order to determine overall susceptibility of the airframe to various threat systems. Use of line-by-line (LBL) techniques for prediction of plume IR signatures is limited due to computational costs. Narrow-band model methods were developed as a compromise between the computational requirements of LBL methods and the inaccuracies of broadband and gray gas methods.

Narrow-band modeling is an approximate technique that attempts to retain enough physics to remain reasonably accurate. While capturing many of the physical phenomena associated with gaseous radiation transfer, most narrow-band models neglect the effect of line Doppler shifting (LDS). LDS is shifting of the entire line profile due to relative velocity between two layers of gas. LDS differs from Doppler line broadening in that line broadening results from the thermal velocity distribution within a gas layer, whereas LDS is the result of large-scale velocity differences between gas layers. The effects of LDS can safely be ignored in many engineering applications because there is little, if any, relative velocity between gas layers. In the case of gas turbine and missile exhausts, however, large relative velocities between exhaust gases and atmosphere are necessary to produce thrust. Observation of exhaust plumes through the atmosphere, then, is a prime example of the need to consider LDS effects.

Presented as Paper 94-2065 at the AIAA/ASME 6th Joint Thermophysics and Heat Transfer Conference, Colorado Springs, CO, June 20–23, 1994; received July 25, 1994; revision received June 5, 1995; accepted for publication June 7, 1995.

*Senior Engineer, Systems Engineering Operations, Aerospace and Communications Group. Member AIAA.
†Regents Professor, George W. Woodruff School of Mechanical Engineering.

The intent of this article is to demonstrate an approximate technique for including LDS effects in a narrow-band model. The technique developed here retains the approach of narrow-band models in that it can be applied to engineering problems without excessive computational cost. The new technique is an improvement over standard band models under conditions where LDS is relevant, but, it retains other inaccuracies that are present in standard band models.

Previous Work

Narrow-band modeling is a well-developed technique described in many texts dealing with gaseous radiative transfer. Ludwig et al.[1] give a comprehensive summary of narrow-band model variations. In addition, Ludwig et al.[1] developed explicit computational procedures for various gases relevant to combustion processes. LDS is ignored, however.

Drakes et al.[2,3] studied the effect of LDS on broadband IR radiation. In particular, LDS was included in a narrow-band model analysis of a conical expansion plume, when viewed broadside. The radial velocity component was sufficient to cause emission from the far side of the flowfield to be shifted toward longer wavelengths relative to emission originating in the near side of the flowfield. The apparent effect could be interpreted as general broadening of the line beyond normal pressure and Doppler broadening.

Drakes et al.[2,3] incorporate LDS effects into a band model in two steps. First, the line Doppler shifted equivalent width was calculated by numerically evaluating

$$W = \int_0^{\infty} \left\{ 1 - \exp\left[-\int_0^S k(\nu - \Delta\nu_D, s)\rho(s)\, ds \right] \right\} d\nu \quad (1)$$

The narrow-band average equivalent width was then determined by the standard integration across the line strength probability distribution function.

The second step involved modifying the inverse line spacing. Lines shifted symmetrically about a nominal line center give the resulting spectrum the appearance of an increased number of lines. Hence, an algebraic function of the ratio of line Doppler shift to the mean line spacing ($\Delta\nu_D/d$) was developed, which increased the inverse line spacing (the number of lines per unit wave number) by a factor of up to 2 when the line Doppler shift was as large as the mean line spacing.

The approach taken by Drakes et al.[2,3] to modify a narrow-band model to include LDS assumes symmetric distribution of gas velocity and other properties along the line of sight (LOS). Therefore, lines will be shifted symmetrically about the nominal line position. However, in the case of a plume being observed at range from near end-on, there will occur a nonsymmetric variation of gas properties along the LOS. The difficulty with the symmetry assumption arises in the modification to the inverse line spacing. Flowfields where the LOSs through the gas are not symmetric will not generate a line distribution like that assumed in the inverse line spacing correction modeled by Drakes et al.[3] The present study avoids the symmetric assumption by making no inherent assumption about the form of the distribution of properties in the gas layers under consideration. No modification to the inverse line spacing parameter will be made as a result.

The procedure of Drakes et al.[2,3] also relies on numerical evaluation of equivalent width. Repeated evaluations of Eq. (1) as the calculation proceeds through gas layers and spectral increments lead to computation times approaching LBL calculations. The problem of excessive run time associated with evaluating Eq. (1) is avoided in the present work by development of an approximation that includes the line Doppler shift as a parameter. The approximation is consistent with use of algebraic functions of optical depth and average linewidths found in narrow-band models.

The effect of LDS is also included in a plume signature model developed by Bernstein et al.[4] Similar to the approach taken by Drakes et al., Bernstein et al. assume that the distribution of velocities along the LOS produce a Gaussian distribution of line Doppler shifts. The Doppler linewidth used in the band model formulation is then modified to include the standard deviation of the line Doppler shift.

Development of the Model

The present model assumes a relationship between the line Doppler shifted equivalent width W_s and the standard equivalent width W_u:

$$W_s = W_u f(Su_e, Su_a, \xi, \gamma_L/\gamma_D|_e, \Delta\nu_D) \quad (2)$$

where f is assumed to be dependent on the optical depth of the emitting layer Su_e and the optical depth of all the layers between the observer and the emitting layer Su_a. Additional parameters in the relation include the ratio of linewidth ratios ξ, the ratio of the line widths for the emitting layer $\gamma_L/\gamma_D|_e$, and the line Doppler shift $\Delta\nu_D$.

The basic narrow-band model uses three parameters to determine equivalent width: 1) the total optical depth Su^*, 2) the averaged Lorentz broadened linewidth γ_L, and 3) the averaged Doppler broadened linewidth γ_D. When calculating W_s, other parameters must be included because the problem inherently involves two gas layers with a relative velocity between them. Thus, the additional parameters given in Eq. (2) are required to adequately describe the physics being modeled. Fortunately, all parameters in Eq. (2), with the exception of $\Delta\nu_D$, are readily available in the standard band model formulation.

The total optical depth used in the standard band model formalism Su^* is the sum of the layer optical depths through the emitting layer, or

$$Su^* = \sum_{i=1}^{N} (Su)_i \quad (3a)$$

$$= Su_e + \sum_{i=1}^{N-1} (Su)_i \quad (3b)$$

$$= Su_e + Su_a \quad (3c)$$

Thus, as the computation progresses, the optical depth of the emitting layer Su_e is the most recent optical depth increment in the summation for total optical depth, and the optical depth of the absorbing layer Su_a is the previous layer's total optical depth.

The relative Voigt line shapes of emitting and averaged absorbing layers are described by ξ and $\gamma_L/\gamma_D|_e$. The ratio of linewidths is used in determination of the Voigt line profile. The relationship between the absorbing layer line shape and the emitting layer line shape is specified by the ratio of the linewidth ratios ξ. Taking the Lorentz linewidth to be[5]

$$\gamma_L(T, P) = \gamma_L(T_0, P_0)(P/P_0)\sqrt{(T_0/T)} \quad (4)$$

the ratio of the half-widths can be reduced to

$$\gamma_L/\gamma_D = (\mathrm{K}P)/(\nu_0 T) \quad (5)$$

where K is a group of constants, dependent only on species. Thus, γ_L/γ_D can be determined from pressure, temperature, and line spectral location. The relationship of line shapes in two layers is characterized by the ratio of linewidth ratios, or

$$\xi = \frac{\gamma_L/\gamma_D|_a}{\gamma_L/\gamma_D|_e} = (P_a/T_a)(T_e/P_e) \quad (6)$$

The final parameter of Eq. (2) is $\Delta\nu_D$. This quantity represents the spectral distance that the emitting layer's line center is shifted relative to the absorbing layer's line center. $\Delta\nu_D$ is determined from the relative velocity component directed parallel to LOS and the line center wave number:

$$\Delta\nu = \nu_0(V/c) \tag{7}$$

The algebraic form of f is constrained by the physics of line formation. For example, the optically thin and optically thick limits constrain the form of f as follows:

$$\lim_{Su^*\to 0} f = 1 \tag{8a}$$

$$\lim_{Su^*\to \infty} f = 1 \tag{8b}$$

$$\lim_{Su^*\to 0} \frac{\partial f}{\partial Su^*} = 0 \tag{8c}$$

$$\lim_{Su^*\to \infty} \frac{\partial f}{\partial Su^*} = 0 \tag{8d}$$

In the case of the optically thin limit, W_s must be identical to W_u, as all energy reaches the observer. At the optically thick limit, the line is saturated over wide spectral regions, making the equivalent width dependent only on optical depth.

The functional dependence of f on $\Delta\nu_D$ must be such that zero relative velocity will result in W_s equal to W_u. This requirement simply ensures that the modified narrow-band model produces the same result as the original narrow-band model when calculating intensity for the condition of no relative velocity.

While some of the constraints on f have been defined, there is insufficient information to define the particular form. Thus, W_s and W_u were determined by the numerical integration of Eq. (1), followed by curve-fitting that met the constraints defined by Eq. (8). In the evaluation of Eq. (1), the Voigt profile approximation proposed by Humlicek[6] was used to determine the spectral absorption coefficient. The numerical integration used 10^5 equally spaced spectral increments spanning ± 1000 line widths (the larger of γ_L and γ_D). The conditions for which the equivalent widths were calculated included three line Doppler shifts ($\Delta\nu_D$ = 0, 7.5×10^{-3} and 15.0×10^{-3} cm^{-1}), three ratio of linewidth ratios (ξ = 1.3, 2.6, and 5.2), and nine emitting layer linewidth ratios ($\gamma_L/\gamma_D|_e = 6.10 \times 10^{-3}$ to 2.44), spanning domination by Doppler broadening to domination by Lorentz broadening. At each combination of $\Delta\nu_D$, ξ, and $\gamma_L/\gamma_D|_e$, equivalent widths were calculated for 10^{-4} cm^{-1} < Su_e < 10^2 cm^{-1} and 200 nondimensionalized absorbing layer optical depths in the range $6.74 \times 10^{-3} \le (Su/\gamma_L)_a \le 3.27 \times 10^6$. Additional combinations of parameters were used as required to provide detail to the form of f.

Figure 1 shows the results of these calculations for a single combination of ξ, $\gamma_L/\gamma_D|_e$, and $\Delta\nu_D$. The f has been plotted as a function of $(Su/\gamma_L)_a$. At very large and very small absorbing layer optical depths, the function f approaches one with a slope approaching zero as expected from the optically thin and thick constraints [Eq. (8)]. The curves of Fig. 1 peak at moderate optical depths for both emitting and absorbing layers. The absorbing layer optical depth at which the peak in f occurs and the magnitude of the peak are dependent on the emitting layer optical depth. Other combinations of ξ, $\gamma_L/\gamma_D|_e$, and $\Delta\nu_D$ produce plots similar to Fig. 1.

The data of Fig. 1 collapses by normalization and coordinate translation. Normalization was accomplished by subtracting one from all values and then dividing the result by the maximum value. Figure 2 shows the data of Fig. 1 plotted in

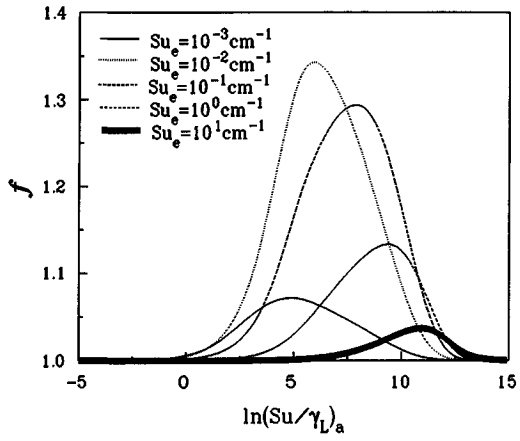

Fig. 1 Ratio of shifted equivalent width to unshifted equivalent width: $\gamma_L/\gamma_D|_e = 1.22 \times 10^{-2}$, $\xi = 2.6$, $\Delta\nu_D = 7.5 \times 10^{-3}$ cm^{-1}.

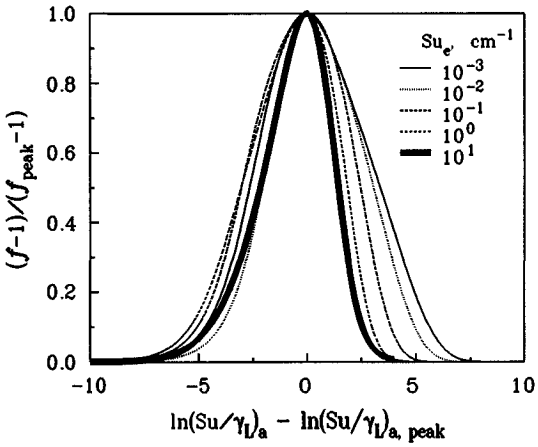

Fig. 2 Normalized ratio of shifted equivalent width to unshifted equivalent width: $\gamma_L/\gamma_D|_e = 1.22 \times 10^{-2}$, $\xi = 2.6$, $\Delta\nu_D = 7.5 \times 10^{-3}$ cm^{-1}.

the new coordinates, $[(f-1)/(f_{\text{peak}}-1)]$ and $[\mathcal{M}(Su/\gamma_L)_a - \mathcal{M}(Su/\gamma_L)_{a,\text{peak}}]$. The function f now has the form

$$f = 1 + (f_{\text{peak}} - 1)g[\mathcal{M}(Su/\gamma_L)_a - \mathcal{M}(Su/\gamma_L)_{a,\text{peak}}] \tag{9}$$

where f_{peak} and $\mathcal{M}(Su/\gamma_L)_{a,\text{peak}}$ are still functions of Su_e, ξ, $\gamma_L/\gamma_D|_e$, and $\Delta\nu_D$. While the process used to arrive at Eq. (9) has not collapsed the data to a single curve, the curves plotted in the new coordinates (Fig. 2) are more similar than the original curves of Fig. 1. As before, other combinations of ξ, $\gamma_L/\gamma_D|_e$, and $\Delta\nu_D$ produce plots similar to Fig. 2.

The shape function g of Eq. (9) has characteristics similar to probability distribution functions. If g is taken to be Gaussian then

$$g(x^*) = \exp(-Ax^{*2}) \tag{10}$$

where

$$x^* = \mathcal{M}\left(\frac{Su}{\gamma_L}\right)_a - \mathcal{M}\left(\frac{Su}{\gamma_L}\right)_{a,\text{peak}} \tag{11}$$

Using this functional form and attempting to determine a single value of A for any single curve of Fig. 2 provided a function that fit the theoretical data well either for $x^* < 0$ or $x^* > 0$, but not the entire range of x^*. Splitting g into two pieces, one for positive x^* (with coefficient A^+) and a second for negative x^* (with coefficient A^-) was successful in fitting the theoretical data.

Once the basic form of f was established, the values of f_{peak}, $\sqrt{(Su/\gamma_L)_{a,peak}}$, A^-, and A^+ were determined for each of the combinations of Su_e, ξ, $\gamma_L/\gamma_D|_e$, and $\Delta\nu_D$. The normalization process directly produces values of f_{peak} and $\sqrt{(Su/\gamma_L)_{a,peak}}$. The shape function coefficients A^- and A^+ had to be determined indirectly, however.

The procedure used to determine A^- and A^+ first linearized the data to be modeled. The theoretical data values were linearized by

$$y_i = \sqrt{\left(\frac{f_i - 1}{f_{peak} - 1}\right)} \tag{12}$$

where f_i is a single point from the equivalent width ratio calculations. The model equation was taken as

$$y_i^* = -Ax_i^{*2} \tag{13}$$

where x_i^* are the values of x^* that correspond to f_i. Minimizing the sum of the squares of the differences between the theoretical data and Eq. (13) leads to

$$A = -\frac{\sum y_i x_i^{*2}}{\sum x_i^{*4}} \tag{14}$$

The summations in Eq. (14) spanned the range $-[5 + \sqrt{(Su/\gamma_L)_{a,peak}}] \le x^* \le 0$ for A^- and $0 \le x^* \le 15.0 - \sqrt{(Su/\gamma_L)_{a,peak}}$ for A^+. The values of the coefficients A^- and A^+ as determined by Eq. (14) are listed in Tables 1 and 2.

The peak ratio of equivalent widths is a function of Su_e, $\gamma_L/\gamma_D|_e$, ξ, and $\Delta\nu_D$. For single values of $\gamma_L/\gamma_D|_e$, ξ, and $\Delta\nu_D$, f_{peak} can be determined as a function of Su_e. Figure 3 is a plot of the data obtained in this fashion for $\gamma_L/\gamma_D|_e = 1.22 \times 10^{-2}$, $\xi = 2.6$, and $\Delta\nu_D = 7.5 \times 10^{-3}$ cm^{-1}. f_{peak} approaches one at very low and very high values of Su_e, with a peak at an intermediate value of Su_e. In order to establish a curve fit, one was subtracted from the known values of f_{peak} and the natural logarithm was taken, resulting in a parabolic-like curve as a function of the natural logarithm of Su_e/γ_L. The parabolic-like curve was then fit with a function of the form

$$\sqrt{(f_{peak} - 1)} = \sum_{n=0}^{6} d_n x^n \tag{15}$$

where

$$x = \sqrt{(Su/\gamma_L)_e} \tag{16}$$

The model for f_{peak} is also shown in Fig. 3. The coefficients d_n of Eq. (15) were determined by using the values of f_{peak} determined through the numerical integration of Eq. (1). The values of the coefficients d_n for all of the calculated conditions are given in Table 3.

The functional dependence of $\sqrt{(Su)_{a,peak}}$ on $\sqrt{(Su/\gamma_D)_e}$ is shown in Fig. 4. The conditions plotted include three $\gamma_L/\gamma_D|_e$

Table 1 Calculated values of the coefficient A^-

$\Delta\nu_D \times 10^3$	$\gamma_L/\gamma_D\|_e$	ξ	$Su_e = 10^{-4}$	$Su_e = 10^{-3}$	$Su_e = 10^{-2}$	$Su_e = 10^{-1}$	$Su_e = 10^{0}$	$Su_e = 10^{1}$	$Su_e = 10^{2}$
7.5	0.0244	1.3	0.07289	0.08832	0.09272	0.07988	0.06413	0.05409	0.08685
7.5	0.0122	2.6	0.06898	0.08437	0.08969	0.06879	0.06096	0.06272	0.08469
7.5	0.0061	5.2	0.06721	0.08264	0.08301	0.06094	0.06518	0.07241	0.08489
7.5	0.2439	1.3	0.07740	0.10664	0.11890	0.10640	0.08267	0.08676	0.11336
7.5	0.1220	2.6	0.07450	0.10355	0.11678	0.09951	0.08774	0.08753	0.09817
7.5	0.0610	5.2	0.07183	0.10072	0.11168	0.09253	0.09164	0.08425	0.09537
7.5	2.4391	1.3	0.05820	0.11192	0.14082	0.13640	0.11868	0.09671	0.13265
7.5	1.2196	2.6	0.05805	0.11161	0.13999	0.13922	0.11546	0.09633	0.12942
7.5	0.6098	5.2	0.05818	0.11183	0.14031	0.13919	0.11723	0.09945	0.12883
15.0	0.0244	1.3	0.06896	0.08442	0.08973	0.07429	0.06316	0.04675	0.07114
15.0	0.0122	2.6	0.06544	0.08095	0.08185	0.06617	0.05953	0.04641	0.05822
15.0	0.0061	5.2	0.06209	0.07748	0.07585	0.06162	0.05029	0.04845	0.06456
15.0	0.2439	1.3	0.07184	0.10083	0.11454	0.10045	0.07494	0.07930	0.11238
15.0	0.1220	2.6	0.06931	0.09815	0.10957	0.09885	0.07721	0.07493	0.09845
15.0	0.0610	5.2	0.06687	0.09544	0.10745	0.09492	0.07481	0.07598	0.08996
15.0	2.4391	1.3	0.05544	0.10818	0.13814	0.13660	0.11093	0.09401	0.12319
15.0	1.2196	2.6	0.05535	0.10795	0.13741	0.13903	0.11372	0.09758	0.12280
15.0	0.6098	5.2	0.05537	0.10798	0.13733	0.13804	0.11492	0.09880	0.11998

Table 2 Calculated values of the coefficient A^+

$\Delta\nu_D \times 10^3$	$\gamma_L/\gamma_D\|_e$	ξ	$Su_e = 10^{-4}$	$Su_e = 10^{-3}$	$Su_e = 10^{-2}$	$Su_e = 10^{-1}$	$Su_e = 10^{0}$	$Su_e = 10^{1}$	$Su_e = 10^{2}$
7.5	0.0244	1.3	0.08800	0.13313	0.16186	0.17742	0.20221	0.26377	0.35457
7.5	0.0122	2.6	0.08835	0.12884	0.16040	0.22757	0.29537	0.33341	0.36846
7.5	0.0061	5.2	0.07666	0.11846	0.15844	0.29566	0.47841	0.47063	0.36763
7.5	0.2439	1.3	0.14298	0.17793	0.19506	0.19044	0.20417	0.26291	0.31740
7.5	0.1220	2.6	0.14271	0.18575	0.20269	0.21734	0.21589	0.25013	0.31864
7.5	0.0610	5.2	0.13377	0.18604	0.20930	0.25375	0.25833	0.25531	0.30107
7.5	2.4391	1.3	0.15186	0.19829	0.23921	0.22515	0.23154	0.24686	0.27666
7.5	1.2196	2.6	0.16060	0.21042	0.25995	0.24518	0.23123	0.24713	0.28999
7.5	0.6098	5.2	0.16706	0.21974	0.27546	0.24929	0.22942	0.23935	0.27494
15.0	0.0244	1.3	0.07483	0.10115	0.12571	0.16459	0.17289	0.19569	0.30264
15.0	0.0122	2.6	0.07377	0.10116	0.13835	0.19777	0.18455	0.21964	0.31890
15.0	0.0061	5.2	0.07161	0.09674	0.14107	0.19812	0.24877	0.31677	0.32073
15.0	0.2439	1.3	0.12221	0.15700	0.18243	0.17940	0.18547	0.25173	0.31712
15.0	0.1220	2.6	0.13360	0.14661	0.17654	0.16395	0.16814	0.22276	0.28217
15.0	0.0610	5.2	0.12067	0.16742	0.20145	0.20804	0.20986	0.24506	0.30063
15.0	2.4391	1.3	0.14254	0.19253	0.22375	0.20637	0.20377	0.24286	0.28016
15.0	1.2196	2.6	0.15168	0.20356	0.23633	0.20814	0.19957	0.23066	0.27140
15.0	0.6098	5.2	0.15896	0.21143	0.24127	0.23527	0.21316	0.22779	0.25737

Table 3 Coefficients d_n of Eq. (15)

$\Delta\nu_D \times 10^3$	$\gamma_L/\gamma_D\|_e$	ξ	d_0	$d_1 \times 10^1$	$d_2 \times 10^1$	$d_3 \times 10^2$	$d_4 \times 10^4$	$d_5 \times 10^4$	$d_6 \times 10^5$
7.5	0.0244	1.3	−4.311	−8.423	12.14	−32.68	391.9	−22.55	5.003
7.5	0.0122	2.6	−4.263	−15.80	14.15	−32.85	344.6	−17.33	3.371
7.5	0.0061	5.2	−4.255	−22.58	15.26	−30.69	276.9	−11.70	1.856
7.5	0.2439	1.3	−3.235	10.04	−0.2994	−3.931	40.95	−0.9920	−0.1647
7.5	0.1220	2.6	−3.868	11.04	0.3664	−7.711	125.0	−8.740	2.326
7.5	0.0610	5.2	−4.728	11.04	1.795	−13.19	214.7	−15.16	3.978
7.5	2.4391	1.3	−4.187	6.495	−1.266	−2.926	10.31	6.877	−5.059
7.5	1.2196	2.6	−4.195	7.049	−1.080	−2.511	4.811	5.290	−3.416
7.5	0.6098	5.2	−4.390	7.701	−0.8617	−2.255	−0.2000	4.605	−2.696
15.0	0.0244	1.3	−4.379	−4.535	9.586	−25.97	311.5	−17.94	3.975
15.0	0.0122	2.6	−4.498	−7.900	9.771	−22.56	233.4	−11.65	2.258
15.0	0.0061	5.2	−4.801	−8.158	8.157	−15.24	117.0	−3.817	0.3636
15.0	0.2439	1.3	−3.039	9.889	−0.2911	−3.022	33.50	−1.446	0.2467
15.0	0.1220	2.6	−3.527	10.38	0.1613	−4.612	63.90	−4.108	1.074
15.0	0.0610	5.2	−4.124	10.33	0.9256	−6.916	96.28	−6.103	1.498
15.0	2.4391	1.3	−3.186	7.113	−1.067	−3.229	4.486	8.136	−5.655
15.0	1.2196	2.6	−3.243	7.556	−0.8366	−2.759	−4.990	7.289	−4.490
15.0	0.6098	5.2	−3.433	8.027	−0.6280	−2.130	−12.41	6.500	−3.563

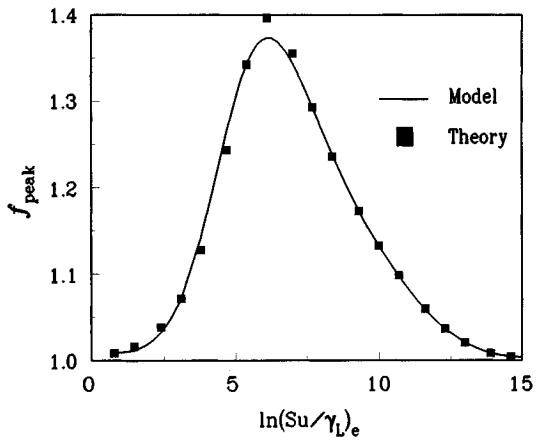

Fig. 3 Peak equivalent width ratio as a function of emitter optical depth: $\gamma_L/\gamma_D|_e = 1.22 \times 10^{-2}$, $\xi = 2.6$, $\Delta\nu_D = 7.5 \times 10^{-3}$ cm^{-1}.

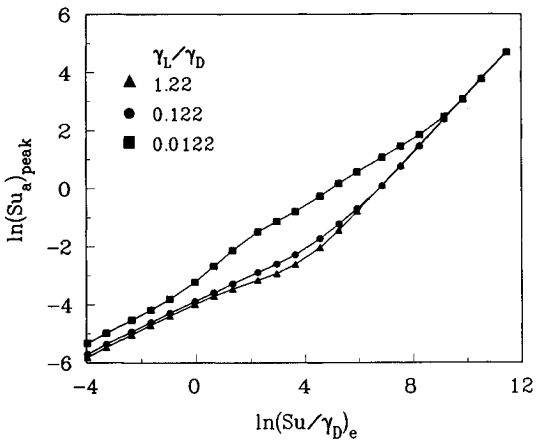

Fig. 4 Absorber optical depth at peak equivalent width ratio as a function of emitter optical depth: $\xi = 2.6$, $\Delta\nu_D = 7.5 \times 10^{-3}$ cm^{-1}.

values (i.e., $\gamma_L/\gamma_D = 1.22 \times 10^{-2}$, 1.22×10^{-1}, and 1.22×10^{0}) at $\xi = 2.6$ and $\Delta\nu_D = 7.5 \times 10^{-3}$ cm^{-1}. Plotted this way, all of the $\eta(Su)_{a,\text{peak}}$ curves collapse to a single line at large values of $\eta(Su/\gamma_D)_e$ (independent of $\gamma_L/\gamma_D|_e$, ξ, and $\Delta\nu_D$). In addition, as $\eta(Su/\gamma_D)_e$ approaches negative infinity, each curve becomes linear. The behavior in the transition region between the two linear regions of each curve is sufficiently complicated to make the determination of a suitable algebraic form a complex problem. Since an efficient means to determine W_s is the overall goal, cubic splines were used to fit the known data. Fortran subroutines for cubic spline curve-fitting based on those given by Press et al.[7] were incorporated into the model for use in determining $\eta(Su)_{a,\text{peak}}$.

Use of cubic spline interpolation scheme is adequate between known data points. Outside the defined range of data, however, an assumption must be made about the shape of the theoretical curves. In the case of $\eta(Su)_{a,\text{peak}}$, the trend for both $\eta(Su/\gamma_D)_e \to \infty$ and $\eta(Su/\gamma_D)_e \to -\infty$ is linear. At the optically thin limit, the linear coefficients from the first defined cubic spline segment were assumed to define the variation of $\eta(Su)_{a,\text{peak}}$ with $\eta(Su/\gamma_D)_e$. Thus for $\eta(Su/\gamma_D)_e \to -\infty$:

$$\eta(Su)_{a,\text{peak}} = b_3[\eta(Su/\gamma_D)_e - \eta(10^{-4}/\gamma_D)] + b_4 \quad (17)$$

Values for both b_3 and b_4 are dependent on γ_D/γ_L, ξ, and $\Delta\nu_D$. At the optically thick limit, a single line was defined for all conditions. Thus, for $\eta(Su/\gamma_D)_e \to \infty$:

$$\eta(Su)_{a,\text{peak}} = \eta(Su/\gamma_D)_e - 6.7591 \quad (18)$$

The values of A^- and A^+ calculated using Eq. (14) have an irregular dependence on Su_e. Despite the irregularity, values of A^- and A^+ must be evaluated at arbitrary values of Su_e, γ_D/γ_L, ξ, and $\Delta\nu_D$. As in the case of $\eta(Su)_{a,\text{peak}}$, a cubic spline curve was chosen as the mechanism for evaluating A^- and A^+ at intermediate values of Su_e.

Examples

The ratio W_s/W_u as a function of $\eta(Su)_a$ is plotted in Fig. 5. Both theoretical [calculated from Eq. (1)] and modeled [Eq. (9)] curves are shown. Figure 6 shows the error in W_s for the modeled data. The largest error in this case indicates that the modeling procedure is within 2% of theoretical over the entire span of absorber optical depths. In typical engineering calculations, a simplified model that approximates theoretical values within a few percent throughout the range of interest might be considered quite successful. In the case of equivalent widths, however, the ultimate objective is the calculation of apparent radiance. Due to the nonlinear relationship between equivalent width and radiance, the error in the apparent radiance may differ significantly from the error in the modeled equivalent width. Small errors in equivalent width can lead to large errors in apparent radiance.

The apparent radiance for a single line calculated using the theoretical and the modeled equivalent widths of Fig. 5 has been plotted in Fig. 7. Here, it is shown that algebraically predicting W_s within 2% of theoretical is insufficient to closely approximate the theoretical apparent radiance for the present

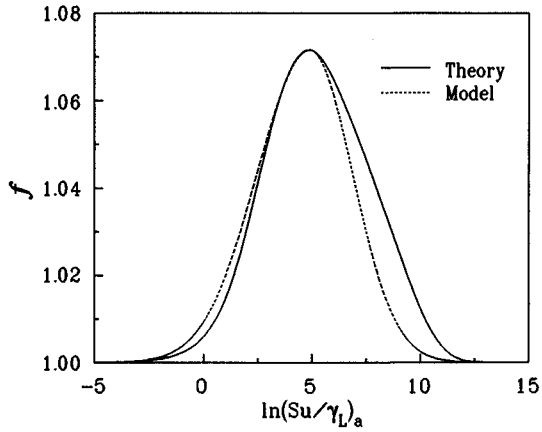

Fig. 5 Comparison of theoretical and predicted ratio of shifted equivalent widths: $Su_e = 10^{-3}$ cm^{-1}, $\gamma_L/\gamma_D|_e = 1.22 \times 10^{-2}$, $\xi = 2.6$, $\Delta\nu_D = 7.5 \times 10^{-3}$ cm^{-1}.

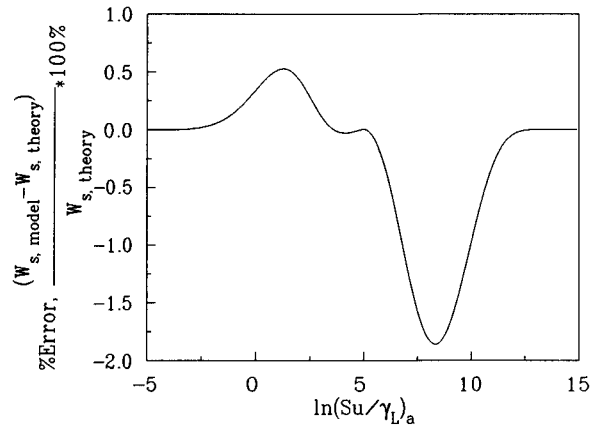

Fig. 6 Percent error in predicted shifted equivalent widths: $Su_e = 10^{-3}$ cm^{-1}, $\gamma_L/\gamma_D|_e = 1.22 \times 10^{-2}$, $\xi = 2.6$, $\Delta\nu_D = 7.5 \times 10^{-3}$ cm^{-1}.

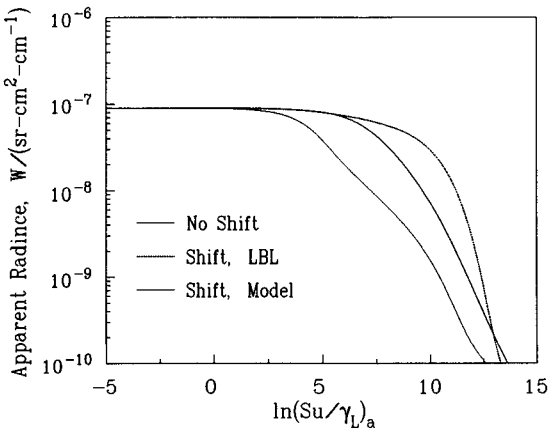

Fig. 7 Single line apparent radiance for shifted and unshifted emission lines: $Su_e = 10^{-3}$ cm^{-1}, $\gamma_L/\gamma_D|_e = 1.22 \times 10^{-2}$, $\xi = 2.6$, $\Delta\nu_D = 7.5 \times 10^{-3}$ cm^{-1}.

set of conditions. The apparent radiance calculated using the model for W_s, however, is a much better approximation for theoretical values than the theoretical apparent radiance without LDS. Under many combinations of conditions, the modeled W_s predicts apparent radiances much closer to theoretical values. In addition, the maximum errors universally occur where the apparent radiance itself has already dropped to a small fraction of the emitted radiance. Here, a small absolute change in radiance causes a large percent error.

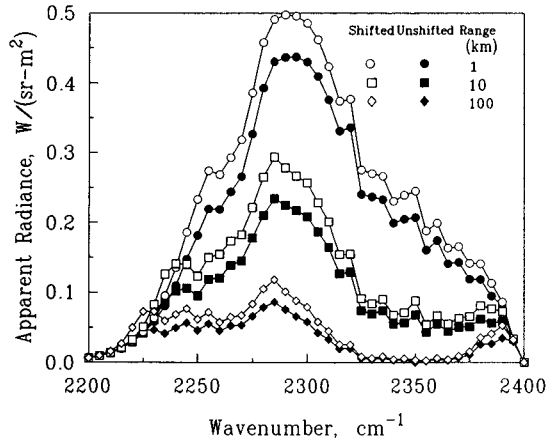

Fig. 8 Apparent spectral radiance, band model method, CO_2 only: $P = 1.09 \times 10^{-3}$ MPa, $\xi = 2.6$, $V = 1$ km/s.

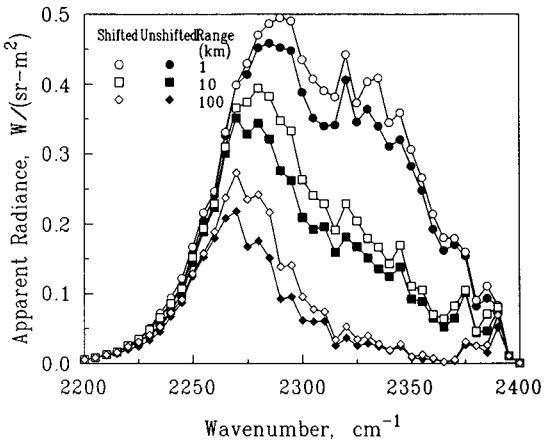

Fig. 9 Apparent spectral radiance, LBL method, CO_2 only: $P = 1.09 \times 10^{-3}$ MPa, $\xi = 2.6$, $V = 1$ km/s.

Finally, the previous calculations apply to a single emission line. There are many thousands of emission and absorption lines in a typical band spectrum, with strengths that vary over many orders of magnitude. While the physical depths of the emitting layer and the absorbing layer are constant from line-to-line, the optical depth varies with the line strength. Thus, for a given combination of layers, there will be lines that have little or no error in apparent radiance. The net effect will be to produce errors in band integrated apparent radiance that are smaller than the peak values shown in Fig. 7.

An example of use of the W_s model in the complete band model, including the multiple line group approximation,[1] can be seen in Fig. 8. Here, apparent radiance is plotted as a function of wave number for three atmospheric layer thicknesses. For comparison, the results of LBL calculations for the same conditions are plotted in Fig. 9 (these calculations used the LBL code developed by Limbaugh et al.[8,9]). The conditions used to calculate apparent radiance values in Figs. 8 and 9 are given in Table 4. For Fig. 8, W_u was obtained from the algebraic model of Ludwig et al.[1]

It can be seen in Figs. 8 and 9 that the effect of LDS increases the intensity reaching an observer at significant ranges. The primary difference between the LBL results and the band model results is due to the more rapid attenuation of the band model calculations, particularly in the region between the red and blue spikes.

The apparent radiance, integrated across the wave band of Figs. 8 and 9, is shown in Fig. 10. Figure 10 clearly shows that the band model results, with or without LDS, are consistently less than the LBL results. Since the integrated ap-

Table 4 Layer properties used in the example

Layer	Plume	Atmosphere
Temperature, K	650	250
Pressure, MPa	0.00109	0.00109
CO_2 mole fraction	0.01	0.00034
Thickness, m	10.0	Varied
Velocity, m/s	1000.0	0.0

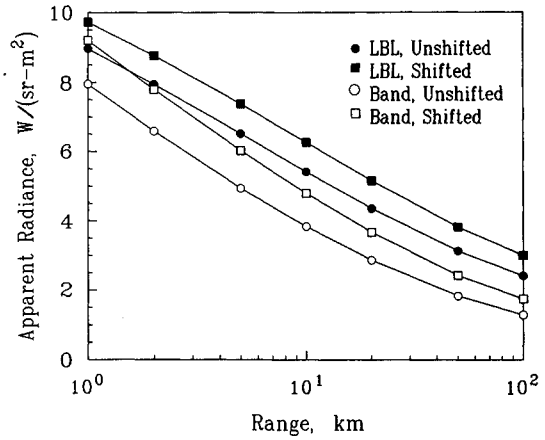

Fig. 10 Comparison of shifted and unshifted band apparent radiance, 2100–2400 cm^{-1}, CO_2 only: P = 1.09 × 10^{-3} MPa, ξ = 2.6, V = 1 km/s.

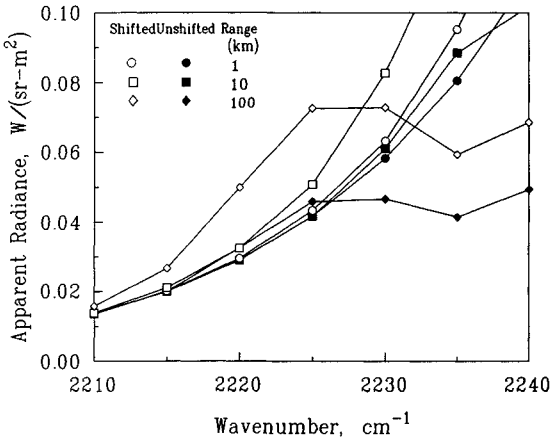

Fig. 11 Apparent spectral radiance, expanded scale, band model method.

parent radiance is consistently in error for the unshifted results, there must be deficiencies, other than the lack of LDS, in the band model formulation. Figure 10 shows however, that the line Doppler shift version of the band model is predicting approximately the correct increase in apparent radiance for the entire wave band.

For one of the atmospheric path lengths shown in Figs. 8–10, the LBL code required 4677 CPU seconds. The modified band model required only 1.5 CPU seconds to calculate the same condition. Calculations were performed on a Sun SPARC-10 computer. Even with potential optimization of the LBL code, the performance benefit of the modified band model will remain.

Application of the line Doppler shift corrections amplifies a second problem with the basic band model. Figure 11 is an expansion of Fig. 8 between 2210–2240 cm^{-1}. At some wave numbers, the apparent radiance increases with atmospheric path length, a violation of the conservation of energy. While the violation of conservation of energy in this spectral region is more pronounced in the line Doppler shifted calculations,

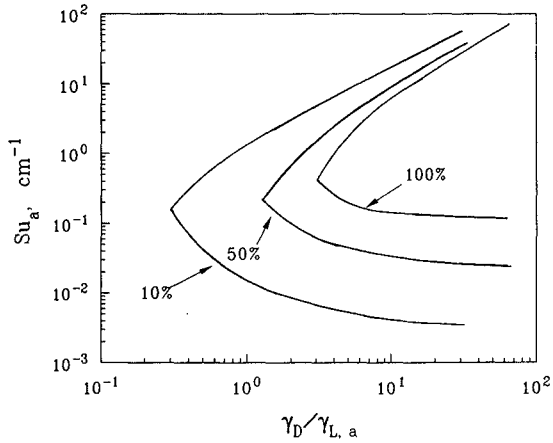

Fig. 12 Percent increase in apparent radiance due to line Doppler shift as a function of absorber linewidth ratio and optical depth: ξ = 2.6, Su_e = 0.1 cm^{-1}, $\Delta\nu_D$ = 7.5 × 10^{-3} cm^{-1}.

it is also present in the standard narrow-band model calculations. Since the W_s model requires a known W_u, it is not possible to avoid magnifying errors in the standard equivalent width model. Analysis of the standard band model indicates that the increase of apparent radiance as the absorber optical depth grows is the result of small errors in the predicted equivalent width, which, in turn, leads to large errors in the apparent radiance.

Conclusions

An algebraic model that can be used to correct narrow-band model formulations to account for LDS has been documented. The algebraic model is dependent on the unshifted equivalent width, the emitting (plume) layer optical depth, the absorbing (atmosphere) layer optical depth, the ratio of linewidths for the emitting layer, the ratio of the linewidth ratios, and the line Doppler shift. In the present study, the unshifted equivalent width was obtained from the model proposed by Ludwig et al.[1] The algebraic model for shifted equivalent width could readily be adapted to work with other standard narrow-band models.

The line Doppler shift correction to the equivalent width should be applied under circumstances where the apparent radiance may be significantly changed. Figure 12 shows the percent increase in apparent radiance as a function of the inverse of absorber linewidth ratio $\gamma_D/\gamma_L|_a$ and absorber optical depth Su_a for a specific emitting layer condition (ξ = 2.6, Su_e = 0.1 cm^{-1}, $\Delta\nu_D$ = 7.5 × 10^{-3} cm^{-1}). The inverse absorber linewidth ratio is roughly proportional to altitude (the pressure variation within the atmosphere causes the Lorentz width to decrease much more rapidly than any variation in the Doppler width), whereas the absorber optical depth is proportional to the absorbing layer physical thickness. Thus, for a given plume signature calculation, Fig. 12 can be used to rapidly determine the need to apply the line Doppler shift correction. Figure 12 shows that correction for LDS is needed only when the line shape is dominated by Doppler broadening and the absorber optical depth is neither very small nor very large.

A snapshot of the capabilities of the algebraic line Doppler shift model has been given in this paper. Space limitations restrict the number of cases that can be presented here. Other examples are available in Ref. 10.

References

[1]Ludwig, C. B., Malkmus, W., Reardon, J. E., and Thomson, J. A., "Handbook of Infrared Radiation from Combustion Gases," NASA SP-3080, 1973.

[2]Drakes, J. A., Hiers, R. S., III, and Reed, R. A., "Doppler Shift

Effects on Infrared Band Models," *Journal of Thermophysics and Heat Transfer*, Vol. 6, No. 1, 1992, pp. 44–47.

[3]Drakes, J. A., and Limbaugh, C. C., "Detailed Examination and Extensions to Infrared Band Model Calculations Including Doppler Shift Effects," AIAA Paper 91-1430, June 1991.

[4]Bernstein, L. S., Sundberg, R. L., Zakin, M. R., Selby, J. E., Freeman, G. N., and Crow, D. R., "Nonequilibrium High-Altitude Rocket Plume Signature Model," *1990 Meeting of the Infrared Information Symposia Specialty Group on Targets, Backgrounds, and Discrimination*, Vol. 1, 213400-37-X(1), March 1990, pp. 47–68.

[5]Clough, S. A., and Kneizys, F. X., "Convolution Algorithm for the Lorentz Function," *Applied Optics*, Vol. 18, No. 13, 1979, pp. 2329–2333.

[6]Humlicek, J., "Optimized Computation of the Voigt and Complex Probability Functions," *Journal of Quantitative Spectroscopy and Radiative Transfer*, Vol. 27, No. 4, 1982, pp. 437–444.

[7]Press, W. H., Teukolsky, S. A., Vettering, W. T., and Flannery, B. P., "Interpolation and Extrapolation," *Numerical Recipes in FORTRAN: The Art of Scientific Computing, Second Edition*, Cambridge Univ. Press, New York, 1992, pp. 107–122.

[8]Limbaugh, C. C., Hiers, R. S., III, and Phillips, W. J., "High-Resolution Spectral Diagnostics in Flows with Mild Vibrational Relaxation," AIAA Paper 89-1676, June 1989.

[9]Limbaugh, C. C., Hiers, R. S., III, and Phillips, W. J., "Spectral Radiative Transfer for the 4.0- to 5.0-μm Bands of CO and CO_2 with Mild Vibrational Relaxation and Doppler Shift," AIAA Paper 90-1782, June 1990.

[10]Hewitt, C. R., Jr., "Technique for Calculating the Effect of Line Doppler Shifting on Transmitted Infrared Radiation," Ph.D. Dissertation, Georgia Inst. of Technology, Atlanta, GA, Nov. 1993.